REVISED 2

Investigation of hydrozincite structure by Infrared and Solid-State NMR Spectroscopy

Roberta Sanna[a], Giovanni De Giudici[b*], Andrea Mariano Scorciapino[a], Costantino Floris[a] and Mariano Casu[a]

Dipartimento di Scienze Chimiche e Geologiche
[a] Complesso Universitario, S.S. 554, I-09042 Monserrato, Cagliari, Italy
[b] Via trentino 51, I-09127, Cagliari, Italy

*corresponding author gbgiudic@unica.it

Abstract

To better understand lattice disorder in hydrozincite, natural hydrozincite samples and synthetic analogues were investigated by XRD, FTIR, ^{13}C MAS and ^{13}C CPMAS NMR. The size of coherent diffraction domains ranges between ~10 nm (Synth1) and ~30 nm (Synth2). FTIR peaks from the antisymmetric CO_3^{2-} stretching ν3 mode were observed at 1383 cm^{-1} and 1515 cm^{-1} in all samples. Peaks due to OH vibrations were observed for all the samples at 3234, 3303 and 3363 cm^{-1}, and were sharp only for the samples having larger crystal domains. The ^{13}C MAS and CPMAS spectra showed a main carbon signal at ~164 ppm in the Synth2 sample, while two main signals were observed at ~164 ppm and ~168 ppm in the Synth1 sample. The intensity ratio of the latter signals were found to be independent of contact time, in the investigated range between 0.2 and 30 ms.

In addition, ^{13}C CP MAS dynamics indicates that the Synth1 sample has shorter $T_{1\rho}$ with respect to Synth2. This indicates a more effective process of spin diffusion of proton magnetization in the former due to different structural properties of Synth1 and Synth2 samples. In addition, chemical shift anisotropy analysis was attributed to a structural change in the carbonate group or hydrogen bonding for Synth1 and Synth2. This was interpreted as a deviation from the ideal structure generated by linear and planar lattice defects and / or grain boundaries.

Keywords: hydrozincite, carbonates, chemical shift anisotropy, nanocrystals

Introduction

Hydrozincite [$Zn_5(CO_3)_2(OH)_6$], is a mineral commonly occurring in the oxidized zones of zinc ores. It is often found as masses or crusts associated with other secondary minerals such as smithsonite, hemimorphite, and aurichalcite (Anthony et al. 2003). Hydrozincite can also precipitate during processes controlled by cyanobacteria (Podda et al. 2000, De Giudici et al. 2009; Medas et al. 2012a, b). More recently, hydrozincite was found to precipitate with hydrocerussite in filamentous fungi (Słaba and Długoński 2011).

The crystal structure of hydrozincite was first studied in a highly crystalline sample by Ghose in 1964 using single crystal X-ray diffraction. The structure is monoclinic with a_0=13.62, b_0=6.30, c_0=5.42 Å, β = 95°50*'*. The space group is *C*2/*m*. Zn occupies two different octahedral sites and one tetrahedral site. The octahedral and tetrahedral sites are in a 3 : 2 ratio. Zinc atoms in tetrahedral coordination occur above holes that are present in the sheets of octahedral zinc atoms. CO_3^{2-} groups bind these sheets parallel to (100). An oxygen atom for each CO_3 group is shared with an octahedrally coordinated Zn, a second oxygen atom is sheared with a tetrahedrally coordinated Zn, and the third oxygen atom is hydrogen bonded to three OH groups.

Ghose (1964) found also that synthetic crystals of hydrozincite have low crystallinity, and speculated that replacement of some carbonate groups holding Tetrahedral-Octahedral-Tetrahedral (T-O-T) groups together would result in stacking disorder. Jambor (1966) and Zabinsky (1966) found that infrared spectra from different hydrozincite specimens differed significantly and showed peak broadening. Such a difference was explained invoking contributions of different plane defects. Conversely, Jambor (1964) and, more recently, Hales and Frost (2007) interpreted IR peak broadening of hydrous zinc carbonate as due to the formation of polymorphs. Lattanzi et al. (2007) and De Giudici et al. (2009) investigated the crystallinity of biologically produced hydrozincite in

comparison with synthetic and geologic reference standards. As pointed out by Medas et al. (2012 b), high precision synchrotron-based X-ray Powder Diffraction (XRPD) patterns of hydrozincites collected in the Rio Naracauli, Sardinia, do not match any known structures of this mineral. In fact, a fairly large difference was recorded for the a_o cell parameter of the geologic hydrozincite (13.59 ± 0.03 Å) and the biologically produced Naracauli hydrozincite (13.832 ± 0.006 Å).

Hydrozincite has been the subject of many studies because of its role in the corrosion of Zn-rich materials (Stoffyn-Egli et al. 1998; Morales and Borges. 2006; Ghosh and Singh 2007), and its involvement in controlling the mobility of zinc both in soils (Uygur and Rimmer 2000) and waters (Mercy et al. 1998; Zuddas and Podda 2005; Wanty et al. 2013). The occurrence of hydrozincite in Zn-contaminated calcareous soils was recently documented by Jacquat et al. (2008). Hydrozincite is a precursor for the preparation of ZnO (Music et al. 2002 and references therein) and it was recently found to be a by-product of Zn-mine-drainage remediation technologies (Perez-Lopez et al. 2011).

Our interest in hydrozincite originated from the discovery, some years ago, that this mineral directly precipitates from the heavy-metal contaminated waters of Rio Naracauli, Sardinia, in association with a biological photosynthetic community, composed of an algae (*Chlorella sp*.) and a cyanobacteria (*Scytonema sp.*; Podda et al. 2000; Zuddas and Podda 2005). At Naracauli Creek, as already shown in the literature, the precipitation of this biomineral results in the reduction of zinc concentration from 348 to 2 mg/L within a few hundred meters downstream. In addition, Pb concentration in the biominerals attains 6500 mg/kg, Cd concentration is 540 mg/kg, together with many other heavy metals detected in high concentration in the Naracauli hydrozincite (see Table 1 in Podda et al. 2000). In a previous study, Transmission Electron Microscopy (TEM) and XRPD analysis indicated a progressive decrease in the size of the particles comparing the biomineral to both the synthetic and geologic samples (De Giudici et al. 2009). Moreover, De Giudici et al. (2009) showed that ^{13}C Magic Angle Spinning (MAS) and Cross Polarization magic angle spinning (CPMAS) NMR spectra have more than one peak for all the investigated samples, despite the fact

that carbon atoms occupy a single crystallographic position in the hydrozincite structure. The additional peaks might reflect the presence of lattice defects typical of nanocrystals.

The disruption of the periodicity in the stacking order leads to measurable effects in the diffraction pattern of the crystal (see Estevez-Rams et al. 2007, and reference therein), and can affect both shape and chemical shift of IR and NMR peaks (see De Giudici et al. 2009, and reference therein). The information about the stacking arrangement contained in the IR and NMR signal, in many cases is not directly available, and can be further "hidden" by other effects such as other structural imperfections (e.g. grain size, line defects, chemical bonding distortion) that contribute to the broadening of the spectral profiles.

The scope of this work is to investigate structure of $[Zn_5(CO_3)_2(OH)_6]$. For this purpose we investigated synthetic hydrozincite samples with different size of single coherent crystal domains by using ^{13}C MAS, CPMAS and Fourier Transform Infrared Spectroscopy (FTIR). These methods are particularly sensitive to small changes in C-O bonding environments, and so represent a suitable method for investigating lattice defects in hydrozincite.

Materials and methods

Samples used in this study

Four specimens of hydrozincite were investigated in this study. Sample Synth1 was synthetized according to protocol reported in Garcia-Clavel et al. (1989) slightly modified. Zinc nitrate was added instead of calcium chloride and synthesis was carried out at 373 K by mixing equal amounts of $(NH_4)_2CO_3$ (Aldrich) solution and $Zn(NO_3)_2{\cdot}6H_2O$ (Aldrich) solution. The precipitate was obtained in about 30 min, then was filtered, washed with cold distilled water and dried at room temperature. A second sample was synthesized according to the hydrothermal procedure described by Music et al. (2002). The aqueous solution was made by adding $Zn(NO_3)*6H_2O$ (Carlo Erba chemicals) with urea (Carlo Erba chemicals). Two autoclaving thermal

112 treatments were applied, first at 60° C for 6 h, and then at 160° C for 20 h. The precipitate obtained
113 was filtered, washed with cold distilled water and dried at room temperature. Hydrothermal
114 hydrozincite is hereafter referred to as Synth2.

115 Besides the two synthetic samples, two museum samples were investigated. One is from the
116 Sa Duchessa Mine (SD), and a second from the Malfidano Mine (MF) respectively, both located in
117 Sardinia, Italy. These samples come from supergene Zn mineralization (calamine), and are more
118 than one million years old (Boni et al. 2003).

119 **X-ray diffraction**

120 XRD was performed with a θ-2θ conventional diffractometer (Phillips X'PERT MPD) with
121 Cu Kα radiation (1.5418 Å). For XRD analysis, 200 mg of each sample was lightly ground in agate
122 mortar and was packed into the sample holder for X-ray diffraction analysis.

123 The particle size of sample was estimated from the full-width at half maximum (FWHM) of
124 the most intense peak according to the Debye-Scherrer formula. The exact FWHM and peak
125 position were obtained by a non linear fitting of the XRD spectra with Log Normal function using
126 the Origin 5.0 program from Microcal Software.

127

128 **Fourier Transformed Infrared Spectroscopy**

129 FTIR spectra were collected in the Mid region from 400 cm^{-1} to 4000 cm^{-1} at 4 cm^{-1} resolution
130 over 64 averaged scans using a Bruker Equinox 55 spectrophotometer. For FTIR analysis of solids,
131 10 mg of solid sample was ground in an agate mortar with 30 mg of KBr and pressed.

132 The overlapping bands observed in the region 2500 – 4000 cm^{-1} were decomposed using the
133 Origin 7 (Microcal) software package. A sum of Gaussian and Lorentzian functions was used
134 throughout with the minimum number of component bands used for the fitting process. Other
135 functions were also examined but the results were inferior. Line widths, intensities, and frequencies

were allowed to vary in the iteration process until reproducible results were obtained with squared correlations (R^2 greater than 0.999).

Nuclear Magnetic Resonance

High-resolution NMR spectra were collected using a Varian Unity Inova spectrometer with a 9.39 T wide-bore Oxford magnet operating at a proton frequency of 399.952 MHz. ^{13}C MAS experiments for solids were performed by packing ~100 mg of lightly ground (in agate mortar) sample into a 4 mm Si_3N_4 rotor, with 7 kHz spin rate, 1200 s recycle time, 6.3 μs pulse length (90°) and 50 kHz spectral window. ^{13}C CPMAS spectra were collected with contact times of 4 ms, and a recycle time of 10 s. Hexamethylbenzene (CH_3 = 17.4 ppm) was used as external reference for ^{13}C chemical shifts. Variable contact time experiments were performed by arraying 17 different contact times from 0.2 to 30 ms. These values were selected in order to investigate a wide range of contact times allowing us to collect any signal from proton that, in hydrozincite environment, can cross polarize. An acquisition time of 50 ms, ^{1}H 90˚ pulse of 4 µs, B1 field strengths of about 36 kHz, 4k data points, a recycle delay of 10 s and 2000 transients were used to acquire all the spectra. The acquisition of the ^{13}C MAS NMR spectra of the Synth1 and Synth2 samples was performed with a probe with 7 mm Si_3N_4 rotors at a spinning rate of 6 kHz for sensitivity reasons. MAS experiments were run with a recycle time of 35 min and 80 transients, 45° pulse lengths (4.5 µs) and 50 kHz bandwidth. The ^{13}C spin-lattice relaxation time in the laboratory frame (T_1) was measured by the Torchia (1978) pulse sequence. The ^{13}C Chemical Shift Anisotropies (CSA) (see Feng et al. 2006 for more details) were determined from analysis of the spinning side band intensities using the WSOLIDS program (Eichele and Wasylishen, 2000).

Results and discussion

XRD

Figure 1 shows the XRD patterns of the samples Synth1 and Synth2. The sharp diffraction lines of sample Synth2 can be indexed as a hydrozincite single phase with a monoclinic structure, according to the experimental (PDF Card 19-1458) and calculated (PDF Card 72-1100) reference patterns. XRD patterns of the Synth1 show broader diffraction lines suggesting a decrease in the size of crystal-coherent domains. The average sizes calculated from the main reflection were ~30 nm, ~19 nm, ~14 nm and ~10 nm for Synth2, MF, SD and Synth1, respectively. It is worth noting that this decrease in the size of crystal coherent domains might depend on the structural evolution of the mineral and/or the crystallization process (Meldrun and Cölfen 2007; De Giudici et al. 2009).

FTIR analysis

The FTIR spectra of the samples MF, SD, Synth1 and Synth2 in the range 400 – 4000 cm^{-1} are shown in Figure 2 and indicate the presence of carbonate groups. The carbonate stretching and bending vibrations were attributed on the basis of the data reported in the literature (Music et al. 2002; Stoilova et al. 2002; Hales and Frost 2007). The four peaks at 1520–1390 cm^{-1} are ascribed to the antisymmetric CO_3^{2-} stretching ν3 mode. The peak at 1050 cm^{-1} is assigned to the ν1 symmetric CO_3^{2-} stretching mode. The strong and sharp peaks at 834 and 705 cm^{-1} are assigned to the ν2 out-of-plane OCO bending mode and to the ν4 antisymmetric OCO bending mode, respectively.

The ν1, ν2, ν3 bands in the Synth1 and SD are broader than observed for MF and Synth2 samples. This has been attributed to lattice defects in hydrozincite (Zabinsky 1966; Music et al. 2002). Music et al. (2002) reported that the splitting into *ν*3 frequency of the two bands at 1512 and 1387 cm^{-1} is dependent on $Zn_5(OH)_6(CO_3)_2$ synthesis.

It should be noted that, spectra of carbonate minerals such as calcite (1421 cm^{-1}), magnesite (1439 cm^{-1}), dolomite (1420 cm^{-1}), and smithsonite (1392 cm^{-1}) are characterized by a single peak, which corresponds to ν_3 degenerate antisymmetric stretching of an undistorted CO_3^{2-} group (White,

1974; Nakamoto, 1997). Indeed, distortion of this group eliminates the degeneracy and results in a double peak at ~1435 and ~1515 cm^{-1} (Sato and Matsuda, 1969; Neumann and Epple 2007). This has been observed in silicate glasses containing dissolved carbon dioxide (Fine and Stolper 1985), ground diopside samples (Kalinkina et al. 2001) and other carbonate minerals such as vaterite (Sato and Matsuda 1969), monohydrocalcite and aragonite (Neumann and Epple 2007).

In the range 2500-4000 cm^{-1} all the samples exhibit a complex pattern of overlapped bands, which can be ascribed to the stretching modes of the hydroxyl groups and water. As shown in Figure 3 the FTIR spectra of the sample Synth2, MF and SD show three main peaks at 3234, 3303 and 3363 cm^{-1}, that have been attributed to the stretching vibrations of the structural OH groups in hydrozincite (Music et al. 2002). In contrast, the FTIR spectrum of the Synth1 sample shows a broad band, instead of the three peaks with the shoulders as observed in the previous samples. The shoulder at higher wavenumbers can be easily detected in Figure 3. In addition, peaks at 3234, 3303 and 3363 cm^{-1} appear to progressively broaden, going from Synth2 to MF, and to the SD sample. Broadening is even more pronounced in the Synth1 sample, where the three bands are not more identifiable and a unique broad band is observed, shifted to higher wavenumbers. All the spectra show shoulders at 3490-3520 cm^{-1} and at 2900-3100 cm^{-1}. The complex overlapping of OH stretching bands can be resolved by the application of band component analysis. This approach has been used in the literature for the simulation of infrared spectra of hydrozincite (Hales and Frost 2007). In order to fit the Synth1 spectrum, the position of the bands attributed to the stretching vibrations of the structural OH groups found in the Synth2 spectrum were set as initial values before the iteration procedure was started.

The FTIR spectra in the 2500 – 4000 cm^{-1} region of Synth1 and Synth2 samples can be fitted with 6 overlapping bands (Fig. 4). Bands at 3375 ± 2, 3303 ± 1, 3234 ± 1 cm^{-1} (line width 110 ± 25, 91 ± 5 and 65 ± 7 cm^{-1} respectively), are found in the Synth2 sample. In the Synth1 sample, 3376 ± 14, 3304 ± 7 and 3239 ± 10 cm^{-1} (line width 130 ± 18, 109 ± 24 and 106 ± 26 cm^{-1} respectively) are found. Results from FTIR fitting does not provide evidence for changes in the band frequency

of OH molecular vibrations. However, it reveals a difference between the line width of the 3239 cm^{-1} (65 ± 7 cm^{-1}) and the 3234 cm^{-1} (106 ± 26 cm^{-1}) bands, while the others do not significantly differ.

Shoulders observed in the 3510-3542 cm^{-1} region might be due to adsorbed and /or hydrogen bonded water. Adsorbed water, indeed, should show a band at 3550 cm^{-1}. The band at 3473 cm^{-1} was attributed to hydrogen bonded water molecules in hydrotalcites by Frost et al. (2003). Broad bands near 3200-3100 cm^{-1} have been tentatively ascribed to adsorbed water in rosasite group minerals and aurichalcite (Reddy and Frost 2007). Ghose (1964) indicated that hydrozincite always contains some adsorbed water on the surface. Moreover, as suggested by Ghose (1964), part of the water molecules could be structural and/or located in channels running parallel to the (001) plane, thus, between the rows of carbonate groups. Therefore, we can speculate that some of the adsorbed and /or hydrogen bonded water identified in the FTIR spectrum should be attributed to water molecules in these hydrozincite channels.

^{13}C NMR analysis

The NMR technique is well known to be sensitive to crystal order and to the presence of lattice defects such as stacking faults and/or polytypes. The chemical shifts provide atomic selectivity for well-ordered systems and is influenced by the local environment, extending to only a few spheres of coordination (Mehring 1983; Engelhardt and Michel 1987).

The ^{13}C MAS spectra of the Synth2, MF and Synth1 hydrozincite samples show overlapping signals in the 162-169 ppm range despite the fact that hydrozincite has only one crystallographically independent site (Fig 5). All the spectra show a main carbon signal at ~164 ppm which is characterized by ^{13}C spin lattice relaxation time in the laboratory frame (T_1), T_1 = 97 ± 15 s for Synth1 sample, T_1 = 5.1 ± 0.7 s for MF sample, T_1 > 150 s for Synth2 sample. In the Synth1

238 sample a second peak can be observed at ~168 ppm with ^{13}C T_1 (89 ± 27 s) not significantly
239 different from that measured at ~164 ppm.

240 The long ^{13}C T_1 of the carbonate carbon in the Synth1 and Synth2 samples is indicative of a
241 rigid atomic lattice, while the lower value of ^{13}C T_1 recorded for the MF sample is due to the
242 presence of paramagnetic impurities (De Giudici et al. 2009). All the spectra show shoulders that
243 decrease in intensity going from Synth1 to MF to Synth2 samples. Stacking faults or polytpysm in
244 the structure of hydrozincite would cause a deviation from the ideal structure and would generate
245 small local distortions resulting in the slight shifts of the carbonate resonance. In addition,
246 nanocrystals such as synthetic hydrozincite have a huge surface area, where crystal truncation
247 produces dangling chemical bonds. In turn, this creates an excess of surface energy that decreases
248 because of aggregation of nanoparticles. For these reasons, De Giudici et al. (2009) ascribed the
249 observed additional peaks to the presence of lattice defects, namely, grain boundaries and stacking
250 modes, in agreement with HRTEM analysis. Figure 5 also shows the ^{13}C MAS spectra obtained
251 with cross polarization (CPMAS) collected at a contact time of 4 ms. No significant differences
252 were observed between MAS and CPMAS spectra.

253 In the ^{1}H-^{13}C cross-polarization experiment, magnetization transfer to the carbon nucleus
254 depends upon the contact time period and is related to other structure-dependent parameters, such as
255 the distance between the two nuclei, the number of protons and the proton relaxation times in the
256 rotating frame (Mehring 1983; Slichter 1989). Only signals from carbon atoms having neighboring
257 hydrogen atom can be collected in the cross-polarization spectrum. Moreover, carbon having a
258 different environment and/or a different mobility are expected to show cross-polarization at
259 different contact times. Thus, the total intensity of the ^{13}C spectra should vary with contact time,
260 depending on how the different signal components behave with respect to contact time. However, in
261 a range between 0.2 and 30 ms, the features of the ^{13}C CPMAS spectra of the investigated samples
262 were found to be independent of contact time, even in the Synth1 sample, where a higher
263 concentration of lattice defects have been observed. Then, we argue that all carbon atoms of our

hydrozincite samples have neighboring hydrogen atoms. It should be noted that non-H-bonded carbonate groups, if present, would have not been cross polarized at short contact times, but could be cross polarized only at longer contact times.

Figures 6 and 7 show the ^{13}C CPMAS spectra of Synth2 and Synth1 samples acquired at two different spinning rates. The spectrum of Synth2 (Fig. 6) shows five bands at 2300 spinning rate , while ten bands are observed at a 13 kHz spinning rate. The spectrum of the Synth1 (Fig. 7) shows a more intricate pattern, characterized by five bands at a 2.3 kHz spinning rate, and each band shows two separate peaks, corresponding to the two isotropic peaks at 164 and 168 ppm. At a 1.4 kHz spinning rate, seven bands are observed (Fig. 7), and again, each band is constituted by two peaks.

The sideband patterns were simulated for each peak to obtain the principal values of the chemical shift anisotropy (CSA) tensors in order to obtain information on the local structure and motions of the carbonate group. The CSA for resonances in ^{13}C CPMAS spectra were determined from the analysis of the Spinning Sidebands (SSB) intensities obtained at low spinning rate.

Least-square fitting of SSB intensities of the Synth2 sample yields the following CSA values for δ_{iso} = 164 ppm: δ_{11} = 218ppm, δ_{22} = 153 ppm, and δ_{33} = 120 ppm. The uncertainty of the principal values, based on four repeated experiments at different spinning rates, was estimated to be about 2 ppm. These values deviate significantly from axial symmetry of carbonate group, in agreement with the differences reported by Ghose (1964) for C-O bond distances in the carbonate group in hydrozincite, C–O1 1.35 Å , C–O2 1.44 Å and for C–O3 1.27 Å.

For the Synth1 sample, CSA values were obtained from the SSB intensities of the two signals at 164 and 168 ppm in the CPMAS spectrum recorded at 1.4 kHz. The CSA values of the signal at δ_{iso} = 164 ppm were δ_{11} = 216 ppm, δ_{22} = 154 ppm, and δ_{33} = 122 pmm. The signals at δ_{iso} = 168 ppm has δ_{11} = 205 ppm, δ_{22} = 182 ppm, and δ_{33} = 115 ppm.

Significant differences can be noted in the CSA values for the signal at 164 and 168 ppm in the Synth1 spectrum**.** In particular δ_{22} differs by 28 ppm between the signal at δ_{iso} = 164 and 168

ppm for Synth1 . On the contrary, significant differences in CSA values for the signal at 164 ppm in the Synth1 and Synth2 CPMAS spectra were not observed.

Previous studies on carbonate and carbonyl compounds indicate that the most shielded principal axis of the CSA, δ_{33}, is usually perpendicular to the carbonate plane, while the less shielded axis, δ_{11}, is placed along the direction defined by the two ether oxygen atoms. This puts the intermediately shielded axis, δ_{22}, along the C=O double bond (Stueber et al. 2002; Robyr et al. 1998; Oas et al. 1987).

It is peculiar that, in our samples, the most affected parameter is the δ_{22} parallel to the C=O bond, which, as reported by Ghose (1964), is involved in hydrogen bonding with the three OH groups. A relationship between hydrogen bond and the δ_{22} parameter has been observed in previous works on carboxyl groups in aminoacids and peptides (Ando et al. 1988, Gu et al 1994, Gardiennet-Doucet et al. 2006). Gu et al. (1994) observed a strong correlation between the δ_{22} values and the strength of hydrogen bonding. Specifically, they observed that the deshielding effect of deprotonation leads to decreased shielding for the δ_{22} element for the protonated carboxyl groups having strong hydrogen bonding. The reverse occurs for the deprotonated carboxylates.

The values of the CSA principal components might be explained by 1) changes in the planarity of the carbonate group, 2) and/or changes in the C-O bond distances induced by deviation from the ideal structure generated by linear and planar lattice defects, grain boundaries and stacking faults, 3) change in H-bonding. In the cases 1 and 2, a variation also of δ_{11} and/or δ_{33} CSA tensors should be expected. On the other hand, significant change in the hydrogen bond is not supported by the analysis of FTIR peaks and the lack of contact–time-dependence observed in ^{13}C CPMAS features of Synth1. Then, a change in H-bonding would be based only on the observed broadening of the FTIR bands in the Synth1 sample. Thus, additional measurement of H position in hydrozincite structure and H bond length are needed to definitely rule out or confirm that changes in H-bonding are responsible for the large difference in δ_{22} CSA tensor element.

315 Additional information can be obtained by ^{13}C CPMAS dynamics spectroscopy (Stejskal and
316 Memory, 1994). In this technique, the intensity data are fitted as a function of the contact time
317 using the standard relationship (Mehring 1983; Slichter 1989):

318 $$I(t) = I_0(1 - T_{CH}/T_{1\rho})^{-1}[\exp(-t/T_{1\rho}) - \exp(-t/T_{CH})] \quad (1)$$

319 where I_0 is the peak intensity, T_{CH} is the cross-polarization time between protons and carbons, and
320 $T_{1\rho}$ is the proton spin lattice relaxation time in the rotating frame, allowing the values for these two
321 characteristic times to be obtained. The least squares curve-fitting are shown in Figure 8, while
322 Table 1 reports the values obtained for T_{CH} and $T_{1\rho}$. The curve fitting was carried out using the
323 intensity (I(t)) of the peak at 164 ppm for the Synth1, MF and Synth2 samples. The intensity of the
324 168 ppm peak was also analyzed for the sample Synth1.

325 The carbonate signal at 164 ppm of the Synth2 and MF samples exhibits fast build-up of the
326 magnetization and a slow relaxation rate, while the Synth1 signal at 164 ppm is characterized by
327 slower build-up of the magnetization and a faster relaxation rate (Fig . 8). The $T_{1\rho}$ data of Synth2
328 sample show a value >100 ms, larger than in the Synth1 sample, 22.04 ms. The large $T_{1\rho}$ value
329 observed in the Synth2 sample is an indication of the rigid conformation and/or an ineffective spin
330 diffusion. However, the carbonate signal of the Synth2 sample is also characterized by large ^{13}C T_1
331 (>150 s) providing an indication of a highly rigid crystal lattice. This is supported also by the SSB
332 pattern observed for both samples at low spinning rate.

333 The Synth1 sample is also characterized by a large ^{13}C T_1 (97 ± 15 s) and SSB pattern
334 similar to that observed for the Synth2 sample. Thus, we argue that the lower $T_{1\rho}$ data measured in
335 the Synth1 sample must be attributed to a more effective spin diffusion of proton magnetization.

336 The T_{CH} value measured for the carbonate signal at 164 ppm is significantly higher for the
337 Synth1 sample, 1.84 ± 0.15 ms, than for the Synth2 and MF samples, 0.65 ± 0.09 ms. The time
338 constant T_{CH} depends on several parameters such as: the distance between the protons and carbon
339 nuclei, the magnitude of the ^{1}H-^{13}C dipolar coupling (it decreases with the number of hydrogen

atoms bound to the carbon atom under observation and or the distance between proton and carbon atoms), and the mobility of a structural fragment bearing the particular carbon atom. The efficiency of CP transfer is also inversely dependent on mobility, thus, a decrease in T_{CH} values would reflect an increase in the fragment rigidity. The slower build-up of the magnetization of the signal at 164 ppm in the Synth1 sample should be an indication of a decrease in the carbonate rigidity and/or the structural fragment, which would be in agreement with the smaller T_1 ^{13}C value observed in this sample. Moreover, the carbonate signal at 168 ppm in the Synth1 sample shows a $T_{1\rho}$ and T_{CH} value (19.16 ± 0.29 ms and 2.12 ± 0.29ms, respectively) not significantly different than those measured at 164 ppm (22.04 ± 1.2 ms and 1.84 ± 0.15 ms, respectively). If the $T_{1\rho}$ parameter is sensitive both to molecular motion and to proton spin diffusion, significantly different values would indicate the presence of dynamic processes that are characterized by different rates but are not averaged by proton spin diffusion, which can be possibly attributed to a certain degree of spatial heterogeneity in the sample. The similar values observed suggest that proton spin diffusion in the Synth1 sample is efficient enough to equilibrate dynamical processes, and that the nearest protons are sufficiently close to produce adequate cross polarization of the carbon atoms. The proton spin diffusion might be also mediated by the presence of water molecules in the channels.

A ^{13}C NMR study of 28 synthetic and natural carbonates including samples of mineralogical and biogenic origin, showed only a small shift range, from166.3 ppm for a synthetic magnesian calcite to 169.9 ppm for aragonite (Papenguth et al. 1989). This relatively small chemical shift variation reflects some change in the structure of the CO_3^{2-} group (Papenguth et al. 1989). On the other hand this relatively narrow range is slightly extended to 163.8 ppm in the scapolite series, where the carbonate group is more distorted than in the simple carbonates (Sherriff et al. 1987). A similar chemical shift value is observed in hydrozincite, as shown, supporting the idea that the carbonate group might be similarly distorted. However a tight correlation between carbonate distortion and ^{13}C chemical shift cannot be invoked. In fact, many examples could violate a general

rule, for example the carbonate groups in vaterite have higher ^{13}C chemical shifts than observed for calcite, but the carbonate group in this mineral is more distorted than in calcite.

Finally, the IR and NMR analysis provided deeper insight on the hydrozincite structure, showing some structural difference in the mineral depending on the synthesis methods. (Ghose 1964; Jambor 1964; Zabynski, 1966; Hales and Frost 2007; De Giudici et al. 2009; Medas et al. 2012b). Specifically, the elongation of the a_0 lattice parameter by more than 10% (Lattanzi et al. 2007) could correspond also to distortion of carbonate groups. In fact, the carbonate groups hold the T-O-T sheet structure together and consequently, a microstructural change of carbonate groups in hydrozincite can be reflected in different layer sequences, in agreement with the observed elongation in the a_o cell parameter observed by Lattanzi et al. (2007) (see also Medas et al. 2012a).

NMR analysis indicates that the Synth1 sample shows shorter $T1_\rho$ with respect to the better cristalline Synth2 sample. This seems to be due to spin diffusion to a reservoir of restrictedly mobile H. Such a change in the H spin diffusion processes might be due to different structural properties of Synth1 and Synth2 samples. These are nanometric size, abundance of both line and planar defects, fusion of nanocrystallites during aggregation processes, presence of chemical dangling bonds, elongation of a_0 lattice parameters. While fairly crystalline samples like Synth2 show a structure similar to the hydrozincite defined by Ghose (1964), poorly crystalline samples like Synth1 have a significantly different structure, likely a polymorph. Based on the observed NMR features, biologically controlled $[Zn_5(CO_3)_2(OH)_6]$ mineralization from Naracauli (De Giudici et al. 2009) has the same structure as the poorly crystalline Synth1 sample.

Acknowledgement

This work was supported by funding from EU project UMBRELLA (grant 226870). Comments from the Associate Editor (Brian Phillips) and criticism of three reviewers were appreciated and useful to improve this work.

References

Ando, S., Ando, I., Shoji, A. and Ozaki, T. (1988) Intermolecular Hydrogen-Bonding Effect on ^{13}C NMR Chemical Shifts of Glycine Residue Carbonyl Carbons of Peptides in the Solid State. Journal of American Chemical Society, 110, 3380-3386.

Anthony, J. W., Bideaux, R. A., Bladh, K. W. and Nichols, M. C. (2003) Handbook of Mineralogy, pp. 791, Mineral Data Publishing, Tucson, Arizona, USA.

Boni, M., Gilg, H.A., Aversa, G., and Balassone, G. (2003) The "calamine" of southwest Sardinia: Geology, mineralogy and stable isotope geochemistry of supergene Zn mineralization. Economic Geology, 98, 731–748.

De Giudici G., Podda F., Sanna R., Musu E., Tombolini R., Cannas C., Musinu A., and Casu M., (2009) Structural properties of biologically controlled hydrozincite: a HR-TEM and NMR spectroscopic study. American Mineralogist, 94, 1698–1706.

Eichele, K. and Wasylishen, R.E. (2000) WSOLIDS. Dalhousie University, Halifax, Canada

Engelhardt, G., and Michel, D. (1987) High-Resolution Solid-State NMR of Silicates and Zeolites, 485 p. Wiley, New York.

Estevez-Rams, E., Penton Madrigal, A., Scardi, P., and Leoni, M., (2007) Powder diffraction characterization of stacking disorder. Zeitschrift fur Kristallographie, Supplement 1 (26), 99-104

Feng J., Reeder, R.J., and Phillips, B.L., (2006) Observation of bicarbonate in calcite by NMR spectroscopy. American Mineralogist, 91, 957–960.

Fine, G., and Stolper, E., (1985) Dissolved carbon dioxide in basaltic glasses: concentrations and speciation. Earth Planetary Science Letter, 76, 263–278.

Frost, R. L. , Martens, W., Ding, Z., Kloprogge, J. T., and Johnson, T. E. (2003) The role of water in synthesised hydrotalcites of formula $MgxZn_{6-x}$ $Cr_2(OH)_{16}(CO_3)\cdot 4H_2O$ and $Ni_xCo_{6-x}Cr_2(OH)_{16}(CO_3)\cdot 4H_2O$ an infrared spectroscopic study. Spectrochimica Acta Part A, 59, 291-302.

Garcia-Clavel, M., Martinez-Lope, M.J. and Casais-Alvarez, M.T. (1989) Thermoanalytical study of the system Pb^{2+}-Zn^{2+} coprecipitated as binary carbonates. Thermochimica Acta, 137, 177–187.

Gardiennet-Doucet, C., Henry, B., and Tekely, P., (2006) Probing the ionisation state of functional groups by chemical shift tensor fingerprints. Progress in Nuclear Magnetic Resonance Spectroscopy 49, 129–149.

Ghose, S. (1964) The crystal structure of hydrozincite, $Zn_5(OH)_6(CO_3)_2$. Acta Crystallographica, 17, 1051−1057.

Ghosh, R., and Singh, D.D.N. (2007) Kinetics, mechanism and characterisation of passive film formed on hot dip galvanized coating exposed in simulated concrete pore solution. Surface and Coating Technology, 201, 7346-7359.

Gu, Z., Zambrano, R. and McDermott, A. (1994) Hydrogen bonding of carboxyl groups in solid-state amino acids and peptides: comparison of carbon chemical shielding, Infrared Frequencies, and Structures, Journal of American Chemical Society, 116, 6368-6372.

Hales, M.C., and Frost, R.L. (2007) Synthesis and vibrational spectroscopic chararacterization of synthetic smithsonite and hydrozincite. Polyhedron, 26, 4955–4962.

Jacquat, O., Voegelin, A., Villard, A., Marcus, M.A. and Kretzschmar, R. (2008) Formation of Zn-rich phyllosilicate, Zn-layered double hydroxide and hydrozincite in contaminated calcareous soils. Geochimica et Cosmochimica Acta, 72, 5037–5054.

Jambor, J.L. (1964) Studies of basic copper and zinc carbonates; Part 1, Synthetic zinc carbonates and their relationship to hydrozincite. Canadian Mineralogist, 8, 92–108.

Jambor, J.L. (1966) Natural and synthetic hydrozincites. Canadian Mineralogist, 8, 652–653.

Kalinkina, E.V., Kalinkin, A.M., Forsling, W., and Makarov, V.N. (2001) Sorption of atmospheric carbon dioxide and structural changes of Ca and Mg silicate minerals during grinding I. Diopside. International Journal of Mineral Processing, 61, 273–288.

Lattanzi, P, Meneghini, C, De Giudici, G, and Podda, F. (2007) Report of experiment 08-02-636. ESRF, Grenoble.

Medas D., Cidu R., Lattanzi P., Podda F, Wanty R.B. and De Giudici G. (2012a) Hydrozincite seasonal precipitation at Naracauli (Sardinia – Italy): Hydrochemical factors and morphological features of the biomineralization process. Applied Geochemistry, 27, 1814-1820.

Medas D., Cidu R., Lattanzi P., Podda F and De Giudici G. (2012b) Natural Biomineralization in the Contaminated Sediment-Water System at the Ingurtosu Abandoned Mine, in E. Kothe and A. Varma (eds.), Bio-Geo Interactions in Metal-Contaminated Soils, Soil Biology 31, p 113-130, Springer-Verlag Berlin Heidelberg.

Mehring, M. (1983) Principles of High Resolution NMR in Solids, 2nd edition, 342 p. Springer-Verlag, New York.

Meldrum, F., and Cölfen, H. (2007) Controlling mineral morphologies and structures in biological and synthetic systems. Chemical Reviews, 108, 4332–4432.

Mercy, M.A., Rock, P.A., Casey, W.H., and Mokarram, M.M. (1998) Gibbs energies of formation for hydrocerussite [$Pb(OH)_2 \cdot (PbCO_3)_2(s)$] and hydrozincite {$[Zn(OH)_2]_3 \cdot (ZnCO_3)_{2(s)}$} at 298 K and 1 bar from electrochemical cell measurements. American Mineralogist, 83, 739–745.

Morales, J.F. and Borges, J. (2006) Atmospheric corrosion in subtropical areas: XRD and electrochemical study of zinc atmospheric corrosion products in the province of Santa Cruz de Tenerife (Canary Islands, Spain). Corrosion Science, 48, 361-371.

Music, S., Popovic, S., Maljkovic, M. and Dragcevic, D. (2002) Influence of synthesis procedure on the formation and properties of zinc oxide. Journal of Alloys and Compounds, 347, 324–332.

Nakamoto, K. (1997) Infrared and raman spectra of inorganic and coordination compounds: Part A. theory and applications in inorganic chemistry. Wiley and Sons, pp 387, New York.

Neumann, M. and Epple, M. (2007) Monohydrocalcite and Its Relationship to Hydrated Amorphous Calcium Carbonate in Biominerals. European Journal of Inorganic Chemistry, 2007, 1953–1957.

Papenguth, H.W., Kirkpatrick, R.J., Montez, B. and Sandberg, P.A. (1989) ^{13}C MAS NMR spectroscopy of inorganic and biogenic carbonate. American Mineralogist, 74, 1152-1158.

Perez-Lopez, R., Macías, F., Caraballo, M.A., Nieto, J.M., Roman-Ross, G., Tucoulou, R. and Ayora, C. (2011) Mineralogy and geochemistry of Zn-rich mine-drainage precipitates from an MgO passive treatment system by synchrotron-based X-ray analysis. Environmental Science and Technology, 45, 7826–7833.

Podda, F., Zuddas, P., Minacci, A., Pepi, M. and Baldi, F. (2000) Heavy metal coprecipitation with hydrozincite [$Zn_5(CO_3)_2(OH)_6$] from mine waters caused by photosynthetic microorganisms. Applied and Environmental Microbiology, 66, 5092–5098.

Oas, T.G., Hartzell, C.J., McMahon, T.J., Drobny, G.P., and Dahlquist, F.W. (1987) The carbonyl ^{13}C chemical shift tensors of five peptides determined from 5N dipole-coupled chemical shift powder patterns. Journal of American Chemical Society, 109, 5956-5962.

Reddy, B.J., and Frost, R.L. (2007) Near infrared spectroscopy of aurichalcite $(Zn,CU^{2+})_5(CO_3)_2(OH)_6$. Journal Near Infrared Spectroscopy, 15, 113-121.

Robyr, P., Utz, M., Gan, Z., Scheurer, C., Tomaselli, M., Suter, U.W. and Ernst R.R. (1998) Orientation of the Chemical Shielding Anisotropy Tensor of the Carbonate Carbon in Diphenyl Carbonate and Its Consequences for NMR Studies on Polycarbonate. Macromolecules 31, 5818-5822.

Sato, M. and Matsuda, S. (1969) Structure of vaterite and infrared spectra, Zeitschrift Fur Kristallographie, 129, S. 405-410.

Sherriff B.L., Grundy, H.D. and Hartman, J.S. (1987) Occupancy of T sites in the scapolites series: a multinuclear NMR study using Magic-Angle-Spinning. Canadian Mineralogist, 25, 717-730.

Słaba, M. and Długoński, J. (2011) Efficient Zn^{2+} and Pb^{2+} uptake by filamentous fungus Paecilomyces marquandii with engagement of metal hydrocarbonates precipitation. International Biodeterioration and Biodegradation, 65, 964 - 960.

Slichter, C.P. (1989) Principles of Magnetic Resonance, 3rd edition, 655 p. Springer Verlag, New York.

Stejskal, E.O. and Memory, J.D. (1994) High-resolution NMR in the solid state. Oxford University Press, pp 192, New York, NY.

Stoffyn-Egli, P., Buckley, D. E. and Clyburne, J. A. C. (1998) Corrosion of brass in a marine environment: mineral products and their relationship to variable oxidation and reduction conditions. Applied Geochemistry, 13, 643-650.

Stoilova, D., Koleva, V. and Vassileva, V. (2002) Infrared study of some synthetic phases of malachite ($Cu_2(OH)_2CO_3$)–hydrozincite ($Zn_5(OH)_6(CO_3)_2$) series. Spectrochimica Acta Part A, 58, 2051–2059.

Stueber, D., Orendt, A.M., Facelli, J.C., Parry, R.W. and David Grant, D.M. (2002) Carbonates, thiocarbonates, and the corresponding monoalkyl derivatives: III.1 The ^{13}C chemical shift tensors in potassium carbonate, bicarbonate and related monomethyl derivatives. Solid State Nuclear Magnetic Resonance, 22, 29–49.

Torchia, D. A. (1978) The measurement of proton-enhanced carbon-13 T_1 values by a method which suppresses artifacts. Journal of Magnetic Resonance, 30, 613-616.

Uygur, V. and Rimmer, D.L. (2000) Reactions of zinc with iron-oxide coated calcite surfaces at alkaline pH. European Journal of Soil Science, 51, 511–516.

Wanty, R.B., Podda, F., De Giudici, G., Cidu, R. and Lattanzi, P. (2013). Zinc isotope and transition-element dynamics accompanying hydrozincite biomineralization in the Rio Naracauli, Sardinia, Italy. Chemical Geology, 337–338 1–10.

White, W.B. (1974). The carbonate minerals. In: Farmer, W.C. Ed., The infrared spectra of minerals. Mineralogical Society, London, pp. 227–284.

Yang, J., Guan, Y., Verhoeven, M.W.G.M., Santen, R.A. van, Li, C., and Hensen, E.J.M. (2009). Basic metal carbonate supported gold nanoparticles: enhanced performance in aerobic alcohol oxidation. Green Chemistry, 11, 322-325.

Zabinsky, W. (1966) The problem of stacking-order in natural hydrozincite. Canadian Mineralogist, 8, 649–652.

Zuddas, P. and Podda, F. (2005) Variations in physico-chemical properties of water associated with bio-precipitation of hydrozincite [$Zn_5(CO_3)_2(OH)_6$] in the waters of Rio Naracauli, Sardinia (Italy). Applied Geochemistry, 20, 507–517.

Table 1 - Cross polarization parameters for Hydrozincite Synth1, Synth2 and Malfidano samples

	Synth1 (168 ppm)	**Synth1 (164 ppm)**	**MF (164 ppm)**	**Synth2 (164 ppm)**
T_{CH} (ms)	**2.1±0.3**	**1.8±0.2**	**0.6±0.1**	**0.6±0.2**
$T_{1\rho}$ (ms)	**19.2±2.9**	**22.0±1.2**	**>100**	**>100**

Captions

Figure 1 – XRD patterns of synthetic (Synth1 and Synth2) samples.

Figure 2 - FTIR spectra of Synth1, SD, MF and Synth2 samples

Figure 3 - FTIR spectra of Synth1, SD, MF and Synth2 samples in the region 2500 – 4000 cm^{-1}

Figure 4 – FTIR spectra of Synth1 and Synth2 samples in the region 2500 – 4000 cm^{-1}. Experimental signals are decomposed into individual Gaussians.

Figure 5 – ^{13}C MAS and $^{13}C/^{1}H$ CPMAS spectra of the Synth1 and Synth2 samples.

Figure 6. Experimental (a, b) slow spinning ^{13}C CPMAS spectra of carbonate group of Synth2 sample and the best-fitting (c). The spinning frequencies were a) 2300 rpm, b) 1400 rpm. The assigned center bands are indicated.

Figure 7. Experimental (a, b) slow spinning ^{13}C CPMAS spectra of carbonate group of Synth1 sample and the best-fitting (c). The spinning frequencies were a) 2300 rpm, b) 1370 rpm. The assigned center bands are indicated.

Figure 8 - Variable contact time ^{13}C CPMAS and non linear least-square fitting for Synth2 at 164 ppm, triangles; Malfidano at 164 ppm, rhombus; Synth1 at 164 ppm, squares; Synth1 at 168 ppm, circles.

Fig. 1

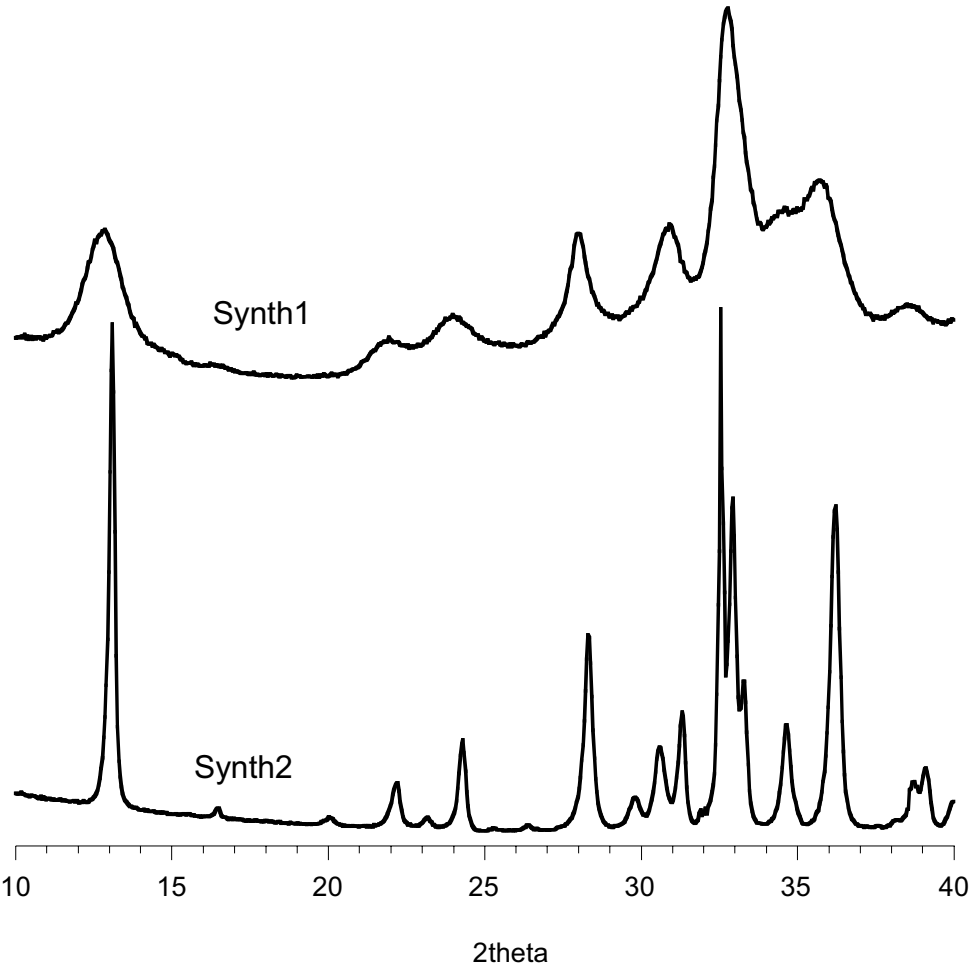

Fig. 2

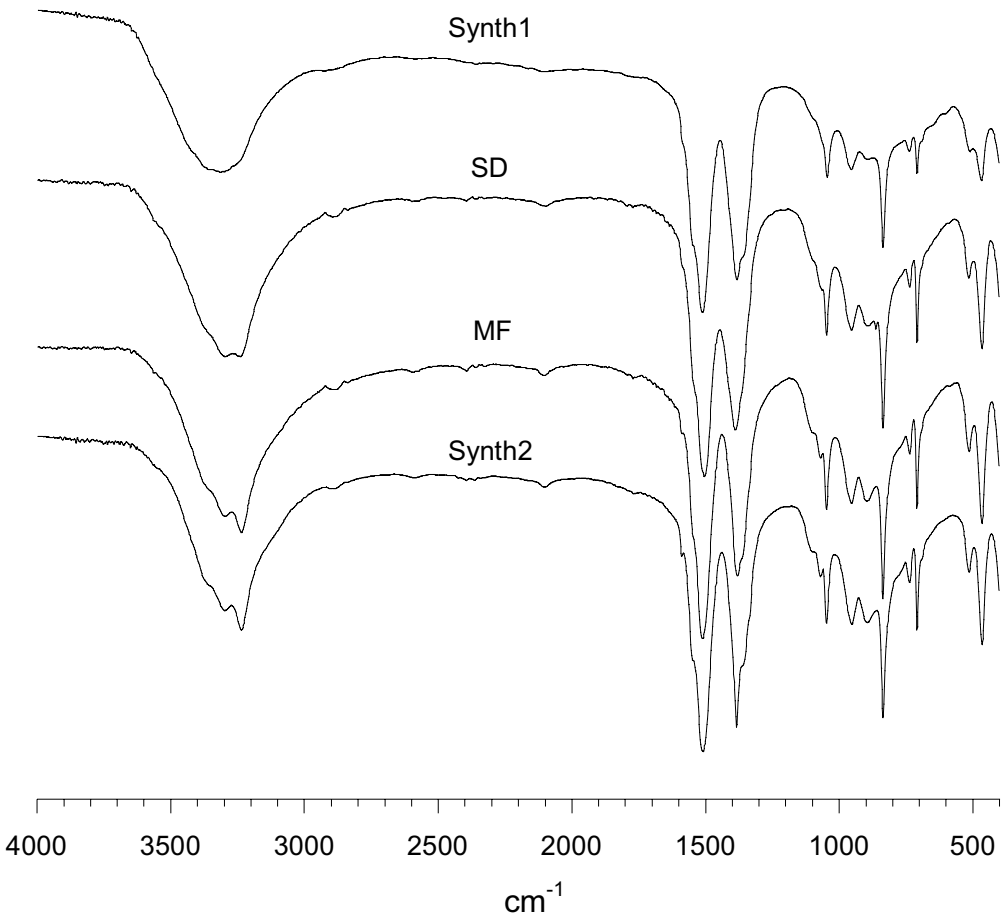
Synth1
SD
MF
Synth2
4000
3500
3000
2500
2000
1500
1000
500
cm-1

Fig. 3

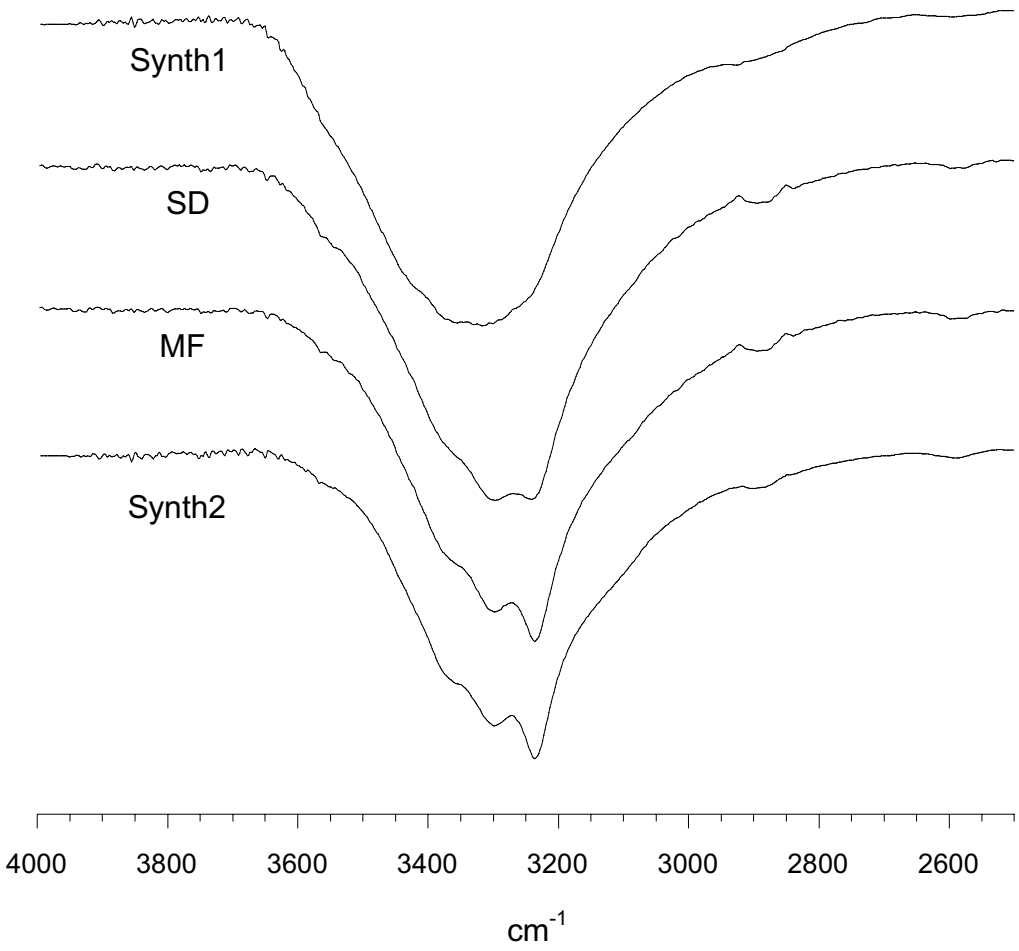
Synth1
SD
MF
Synth2
4000
3800
3600
3400
3200
3000
2800
2600
cm-1

Fig. 4

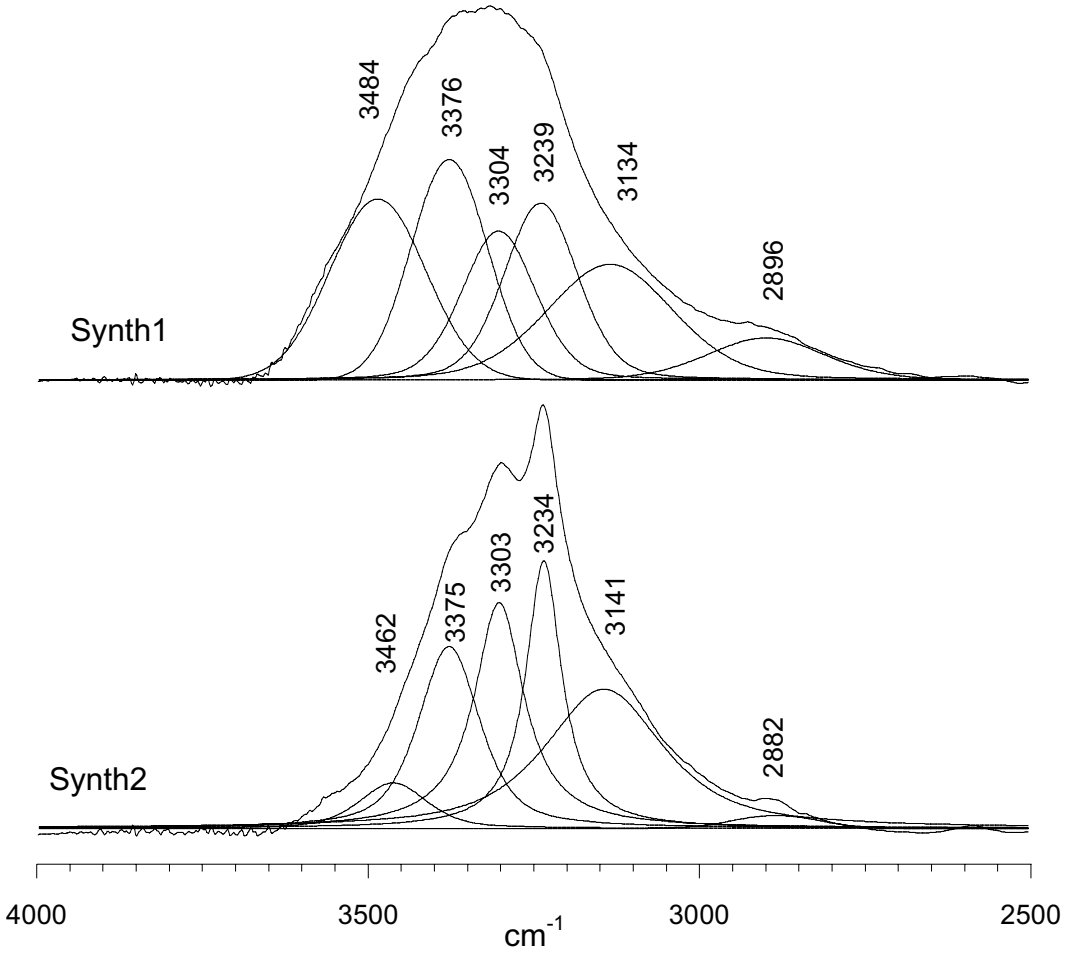
3484
3376
3304
3239
3134
2896
Synth1
3462
3375
3303
3234
3141
2882
Synth2
4000
3500
3000
2500
cm-1

Fig. 5

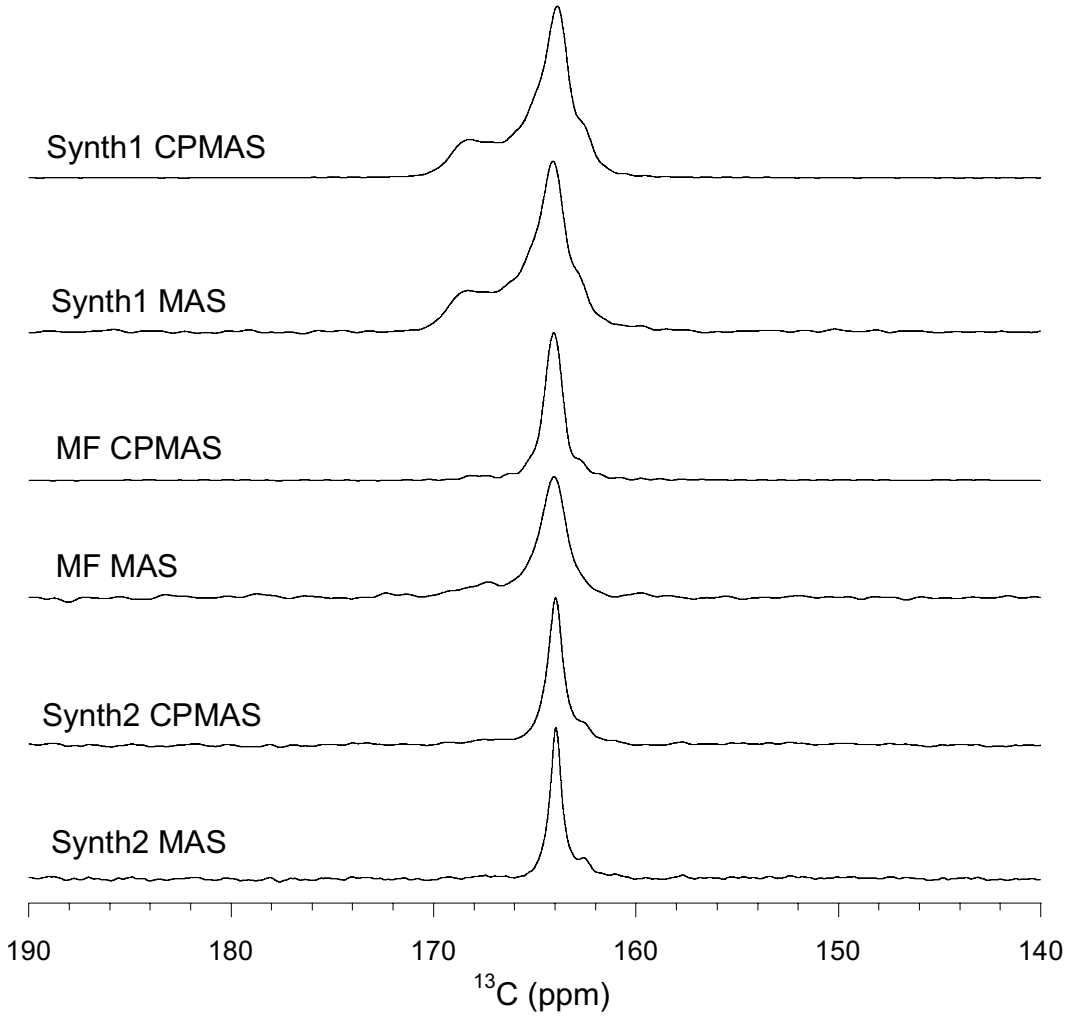
Synth1 CPMAS
Synth1 MAS
MF CPMAS
MF MAS
Synth2 CPMAS
Synth2 MAS
190
180
170
160
150
140
^{13}C (ppm)

Fig. 6

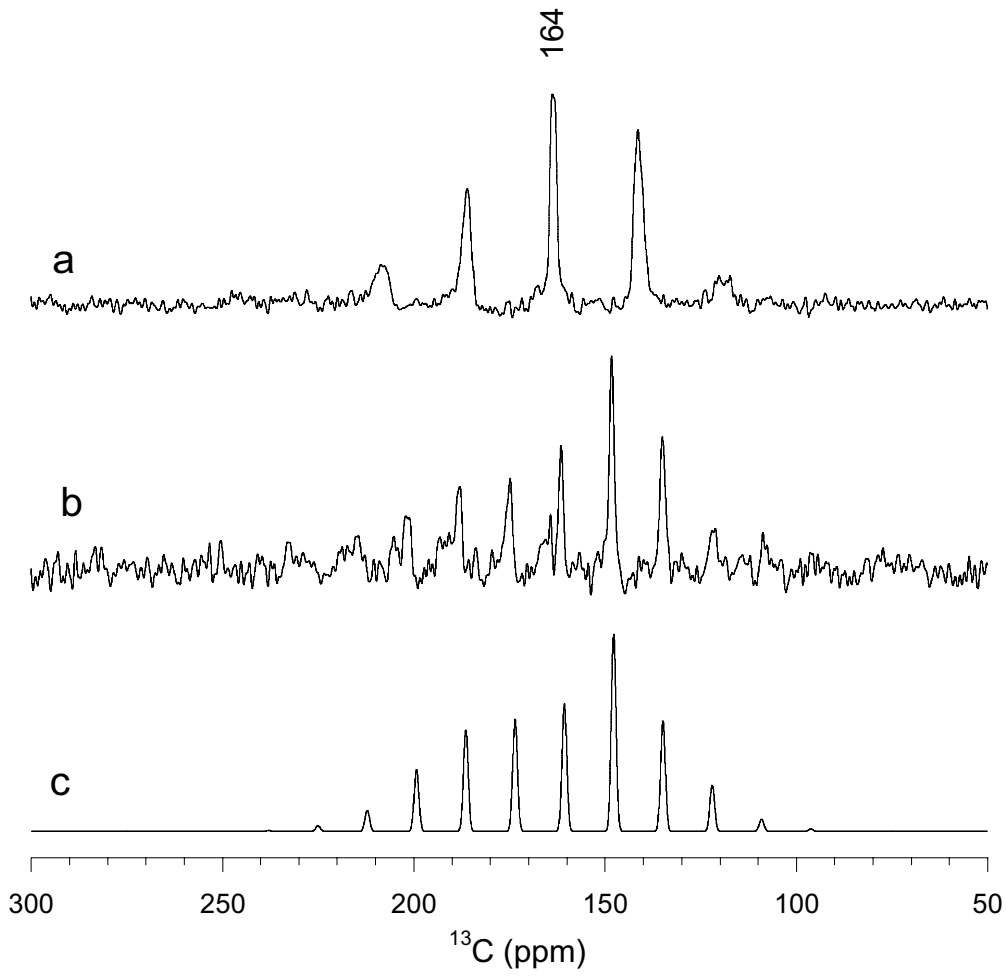

Fig. 7

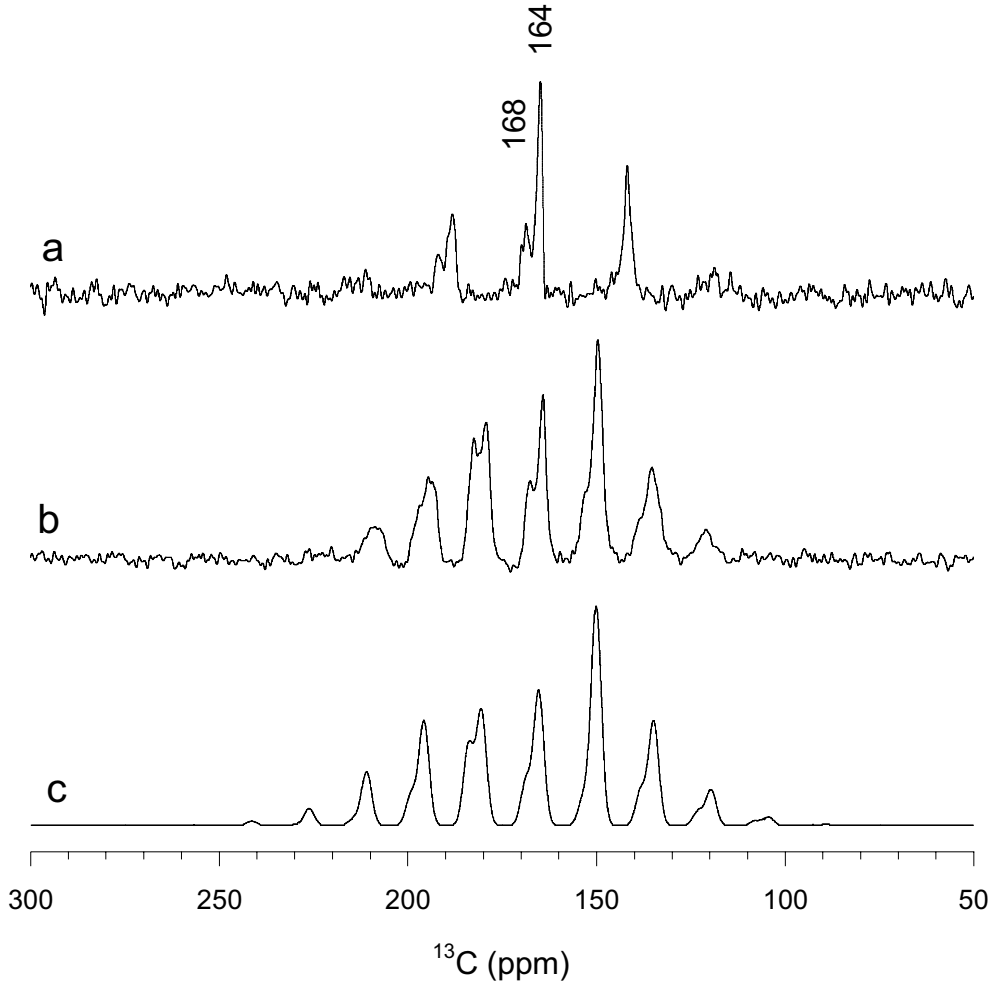

Fig. 8

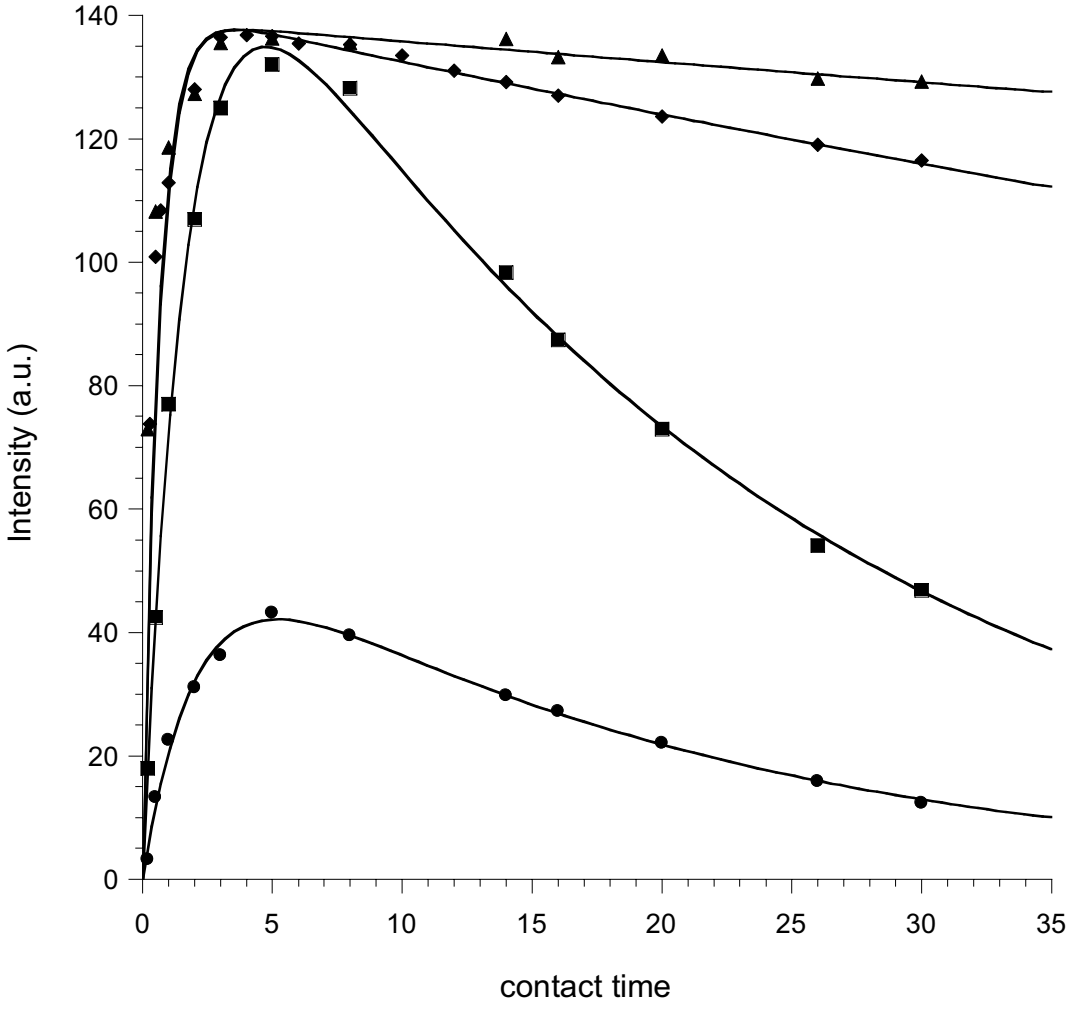
Intensity (a.u.)
contact time
0
20
40
60
80
100
120
140
0
5
10
15
20
25
30
35